Mesoscopic structural organization in fluorinated pyrrolidinium-based room temperature ionic liquids.

F. Lo Celso[a], G. B. Appetecchi[b], E. Simonetti [b], U. Keiderling[c], L. Gontrani[d], A. Triolo[e] and O. Russina[f,*]

[a] Dipartimento di Fisica e Chimica, Università di Palermo, Palermo, Italy.

[b.] ENEA, Laboratory SSPT-PROMAS-MATPRO, Rome, Italy.

[c.] Soft Matter and Functional Materials, Helmholtz-Zentrum für Materialien und Energie GmbH, Berlin, Germany

[d.] Dipartimento di Chimica "Giacomo Ciamician", Bologna, Italy

[e.] Laboratorio Liquidi Ionici, Istituto Struttura della Materia, Consiglio Nazionale delle Ricerche, (ISM-CNR) Rome, Italy

[f.] Department of Chemistry, University of Rome Sapienza, Rome, Italy

[*] olga.russina@uniroma1.it

Abstract.

In this contribution the microscopic and mesoscopic structural organization in a series of fluorinated room temperature ionic liquids, based on *N*-methyl-*N*-alkylpyrrolidinium cations and on bis(perfluoroalkylsulfonyl)imide anions, is investigated, using a synergy of experimental (X-ray and Neutron scattering) and computational (Molecular Dynamics) techniques. The proposed ionic liquids are of high interest as electrolyte media for lithium battery applications. Together with information on their good ion transport properties in conjunction with low viscosity, we also describe the existence of nm-scale spatial organization induced by the segregation of fluorous moieties into domains. This study shows the strong complementarity between X-ray/neutron scattering in detecting the complex segregated morphology in these systems at mesoscopic spatial scales and MD simulations in successfully delivering a robust description of the segregated morphology at atomistic level.

Introduction

Lithium battery systems are excellent candidates for the next generation electrochemical storage systems [1,2] due to their high gravimetrical and volumetric energy values, i.e., five and two times larger than the Pb-acid and NiMH ones, respectively. However, the use of volatile and flammable organic compounds as electrolyte components has been, so far, preventing their development and commercialization in large-scale applications such as automotive, storage from renewable sources, load levelling, smart grids, etc.

Ionic liquids (ILs), salts that are molten at room temperature because of the asymmetry and steric hindrance of their constituting ions [3,4], are blowing-up as innovative class of fluids for a wide variety of electrochemical applications since their unique properties and peculiarities [5]. Basically, they are proposed as "non-volatile" and "non-flammable" solvents with the potential to replace the organic ones [6]. In this scenario, ILs are expected to enhance the safety of the lithium batteries [7]. Also, they have shown to be appealing for post Li-ion systems as Li/S [8], Li/O_2 [9] as well as sodium batteries [10]. Suitable ILs for these kinds of electrochemical energy storage systems are generally composed by tetraalkylammonium or imidazolium or pyrrolidinium and piperidinium cations and perfluoroalkylsulfonylimide anions.

It is well known that the knowledge of the IL ionic structural organization, together with a careful determination of their physicochemical properties, is a fundamental issue aiming at their employment in practical applications. The optimal formulation for ionic liquid electrolytes is strongly correlated to the chemistry and the operating conditions of the final device [6]. In previous structural investigations [11] we have observed the development of mesoscopic scale segregated domains in piperidinium-based ionic liquids upon increasing the cation alkyl chain length. Small Angle X-ray and Neutron Scattering measurements [12], carried out on imidazolium ionic liquids with different alkyl chain lengths, have indicated high level of structural complexity as a consequence of a morphology with hierarchical features at both spatial and temporal scales. Russina *et al*. [13] have shown, through X-ray and NOE-NMR data, the ability of ionic liquids bearing medium length fluorous tails, of tails self-assembling into fluorinated mesoscopic size domains, which simultaneously coexist with charged polar matrices and lipophilic alkyl chain clusters, at least at low enough temperature. Results from ab initio calculations, carried out on other pyrrolidinium-based ILs, are in agreement with the heteronuclear NOE measurements, which show anion interactions with the cation ring [14]. The spatial segregation of fluorinated chains, in asymmetric bis(perfluoroalkylsulfonyl)imide anions, into nm-sized heterogeneities was also evidenced by Lo Celso *et al*. [15,16] through small angle X-ray and neutron scattering. Before that, experimental X-ray scattering experiments [17] and Molecular Dynamics simulations[18] in protic

ILs with fluorinated chains showed related observations, although influenced by the strong hydrogen bonding interactions between opposite ions. This issue, in combination with the established micro-segregation of side alkyl chains, opens to the concept of triphilic ILs, whose technological applications are not fully developed, yet [19]. DFT calculations and low-frequency mechanical experiments by Palumbo *et al*. [20] have confirmed the occurrence of a relaxation process, attributed to the ions motion, which can be described by a hopping model between non-equivalent configurations, this highlighting the role of the anion conformers.

The structural organization of the IL ions influences the physicochemical properties themselves at macroscopic level. In particular, the thermal and ion transport characteristics are very important for screening among different IL families and/or choosing a proper IL to be addressed to particular devices and/or particular operating conditions. For instance, the formation of nanoaggregates affects the melting temperature [11,21] as well as the cation-anion interactions influence the viscosity and, therefore, the ion transport properties of the ILs [22,23].

In the present work, we have focused the investigation on the bis(fluorosulfonyl)imide (FSI, $[IM_{00}]$, where the 00 indicates the number of carbon atoms bearing fluorine atoms at the two sides of the imide), bis(trifluoromethylsulfonyl)imide (TFSI, $[IM_{11}]$), bis(pentafluoroethylsulfonyl)imide (BETI, $[IM_{22}]$) and (trifluoromethylsulfonyl)(nonafluorobutylsulfonyl)imide ($[IM_{14}]$) anions and the *N*-methyl-*N*-propylpyrrolidinium ($[pyr_{13}]$) cation: $[pyr_{13}][IM_{00}]$, $[pyr_{13}][IM_{11}]$, $[pyr_{13}][IM_{22}]$, $[pyr_{13}][IM_{14}]$, respectively. Together with these ILs, also selected other samples were considered, namely $[pyr_{11}][IM_{14}]$ and $[pyr_{14}][IM_{14}]$, for the sake of comparison, but a more detailed description of these latter salts will follow in a separate communication.

Several studies appeared in the last few years focusing on the properties of these or related fluorinated ILs. Fluorinated ILs have been described in previous works [24–28] where different structural properties have been reported. Since the first structural study by Shen and coworkers [17] focused on a fluorinated protic ionic liquid, a subsequent Molecular Dynamics investigation from the Margulis group appeared [18], where the concept of triphilic ionic liquids that we proposed in our first study[13] has been atomistically described. More recently a series of Molecular Dynamics studies by Canongia Lopes and coworkers appeared [29–32], proposing, on the basis of computational work, a scenario where alkyl domains and fluorous ones tend to segregate from the charged three-dimensional network. Although not focusing on fluorinated anions that lead to the formation of fluorous domains, several studies have been dedicated to the exploration of structural properties in pyrrolidinium-based ILs, merging diffraction and computational techniques [33–38]. These studies revealed the existence of a significant polar/apolar alternation related to the segregation of alkyl chains where they are longer than butyl (no experimental data is available for

the case of pentyl chains), in the case of [pyr_{1x}][IM_{11}], as fingerprinted by the existence of a low Q peaks centred at Q_I (such a position being dependent on the side alkyl chain length). Higher Q peaks (Q_{II} and Q_{III} in order of increasing Q position) have also been detected. This behaviour resembles the one observed experimentally by several groups in the last decade on a variety of ILs [13,39–56]. Santos et al. studied [pyr_{1x}][IM_{11}] ILs and monitored the temperature dependence of peaks centred at Q_{II} and Q_{III} [33]. Li et al. studied the temperature dependence of the peak centered at Q_I in [pyr_{1x}][IM_{11}] ILs [34]. Sharma et al. [37] and Pilar et al. [38] studied the effect of hydrostatic pressure on the structural organization in a series of [pyr_{1x}][IM_{11}] ILs, showing how high pressure can deform the mesoscopic organization in this class of ILs [57,58].

In this contribution, we report on a series of structural features of a specific class of pyrrolidinium-based ILs, bearing bis(perfluoroalkylsulfonyl)imide anions, as well as the (nonafluorobutylsulfonyl)(trifluoromethylsulfonyl)imide anion, with high potential for electrochemical applications. Using the synergy between X-ray and neutron scattering we reveal specific diffraction features that point to the existence of nanoscale segregated fluorous domains in ILs bearing long enough side fluorous tail. These results can be straightforwardly interpreted in terms of the mentioned morphology, but we also developed a series of Molecular Dynamics simulations aiming at quantitatively reproducing the experimental structural features and, consequently, to accessing morphological details at atomistic level.

Experimental

Synthesis of ionic liquids

The pyrrolidinium-based ionic liquids were synthesized and purified through routes previously developed at ENEA and described in details elsewhere [59,60]. The chemicals, i.e., *N*-methylipyrrolidine (Sigma-Aldrich, 98 wt.%), 1-bromopropane (Sigma-Aldrich, 99 wt.%), sodium bis(fluorosulfonyl)imide NaFSI (Solvionic, battery grade, > 99.9 wt.%), lithium bis(trifluoromethylsulfonyl)imide LiTFSI (3M, battery grade, > 99.9 wt.%), lithium bis(pentafluoroethylsulfonyl)imide LiBETI (3M, battery grade, > 99.9 wt.%), acidic (nonafluorobutylsulfonyl)(trifluoromethylsulfonyl)imide HIM_{14} (3M, 60 wt.% water solution) were used as received. Activated carbon (Darco-G60, Sigma-Aldrich) and alumina (acidic, Brockmann I, Sigma-Aldrich), used in the purification process, were previously rinsed in deionized water according to a route reported elsewhere [60]. Deionized water, used as the processing solvent, was obtained with a Millipore ion-exchange resin deionizer.

The *N*-methyl-*N*-propylpyrrolidinium bromide precursor, $[pyr_{13}][Br]$, was synthesized by reacting *N*-methylipyrrolidine, previously dissolved in deionized water, with the appropriate amount of 1-bromopropane. Then, the precursor (in aqueous solution) was purified through activated carbon and acidic alumina, obtaining a clear and colourless liquid fraction. The sorbent materials, separated by vacuum filtration, were rinsed with deionized water to recover the trapped precursor. The pyrrolidinium ionic liquids were obtained by reacting (anion exchange) the aqueous $[pyr_{13}][Br]$ with the suitable stoichiometric amount of NaFSI (or LiTFSI or LiBETI or HIM_{14}), giving water-insoluble ionic liquid and hydrophilic NaBr (or LiBr or HBr). After 1 hour mixing, phase separation was allowed. The ionic liquid (separated by the aqueous phase) was rinsed with deionized water to remove the NaBr (or LiBr or HBr) and NaFSI (or LiTFSI or LiBETI or HIM_{14}) residual amounts, and then vacuum dried at 90 °C (rotary evaporator) and at 120 °C (glass oven).

The lithium, bromide and moisture content was checked by atomic absorption analysis (SpetcrAA mod. 220 atomic absorption Spectrometer), X-ray fluorescence spectrometry (Shimadzu energy-dispersion EDX-720 spectrometer) and Karl-Fisher titrator (Mettler Toledo DL32, located in a dry room), respectively.

Small-Wide Angle X-ray Scattering.

High-energy Angle X-ray scattering data were collected at beamline BL04B2 SPring-8 (Japan Synchrotron Radiation Research Institute, JASRI, Japan). [61–63] Measurements were conducted at

ambient conditions. A monochromatized X-ray (61.6 keV) was obtained using a Si(220) monochromator. The observed scattering intensity of the X-ray was corrected for absorption, polarization, and incoherent scatterings [64] to obtain coherent scattering intensities.

High-energy X-ray scattering patterns were also collected at the Advanced Photon Sources (APS) beamline 11-ID-C on samples of $[pyr_{11}][IM_{14}]$ and $[pyr_{14}][IM_{14}]$. The X-ray wavelength was 0.10801 $Å^{-1}$. Sample-to-detector distance is calibrated using the powder diffraction pattern from CeO_2 and is typically about 486 mm, allowing the access to scattering data in the range of scattering vector $Q = 4\pi \sin\theta/\lambda$ between 0.2 and 20 $Å^{-1}$. Corrected X-ray intensity I(Q) was obtained using the Fit2D software.[65] The static structure factor S(Q) was obtained using PDFgetX2 software, that accounts for background subtraction, Compton scattering and oblique incidence angles.[66]

Small Angle Neutron Scattering.

Small Angle Neutron Scattering experiments (SANS) measurements were performed at the small-angle scattering instrument V4 which is placed in the cold neutron guide of Helmholtz-Zentrum Berlin (HZB). The magnitude of the scattering vector is defined as $Q = (4\pi/\lambda)(\sin\theta)$ with λ being the wavelength and 2θ the scattering angle. The measured neutron flux of the V4 is ~10^6 $cm^{-2}.s^{-1}$ for the wavelength used, $\lambda = 4.5$ Å.[67] The scattering data was obtained at one sample detector distance of 1.0 m, which yields a total momentum transfer range of 0.5 $nm^{-1} < Q < 8$ nm^{-1}. For further information regarding the V4 instrument and its resolution the reader is referred to references [67,68]. The sample was placed into a circular quartz cuvette with inner spacing of 1 mm and placed in the beam for measurement. A Cd aperture of 13 mm was used for the scattering measurements. The 2D scattering data were reduced to a scattering curve ($d\Sigma/d\Omega(Q)$ *vs*. Q; hereinafter indicated as I(Q) vs Q) by means of the BerSANS software. The raw data is then corrected for transmission, the quartz cell background scattering subtracted and converted to absolute units taking into account the scattering from water.[69]

Molecular Dynamics Simulation.

Molecular dynamic simulations were performed using the GROMACS 5.1.1 package [70,71]. Interactions were described using an all-atoms potential [72–75]. The simulations were performed using a cubic box with 1120 ($[Im_{00}]$), 960 ($[Im_{11}]$), 850 ($[Im_{22}]$) and 800 ($[Im_{14}]$) ion pairs, where periodic boundary conditions were applied. Force field parameter files and initial configuration were created by DLPGEN software [76]; initial density was fixed 10% higher than the experimental one. The equilibration procedure was done in several steps, starting from a series of NPT simulation at high temperatures and scaled partial charges, followed by lowering progressively the temperature

and increasing the charges to their final value until an equilibrated system was obtained at 298.15 K and 1 bar, after a 15 ns run. This procedure led to a simulation box with side length ~75 Å. After the equilibration phase, the system was run for a total of 20 (70 for [pyr_{13}][IM_{14}]) ns for a production run, and then the trajectory of the last 1 ns was saved at a frequency of 1 ps for calculation of the structural properties. The simulations were always checked versus the experimental density and the energy profile. During the production runs for the temperature coupling, we used a velocity rescaling thermostat [77] (with a time coupling constant of 0.1 ps), while for the pressure coupling, we used a Parrinello–Rahman barostat [78] (1 ps for the relaxation constant). The Leap-Frog algorithm with a 1 fs time step was used for integrating the equations of motion. Cut-offs for the Lennard- Jones and real space part of the Coulombic interactions were set to 15 Å. For the electrostatic interactions, the Particle Mesh Ewald (PME) summation method[79,80] was used, with an interpolation order of 6 and 0.08 nm of FFT grid spacing. Selected graphs were done using Matplotlib [81]. Weighted and partial structure factors were computed by using in-house developed software, accordingly to text book formulas as highlighted in Margulis's work[82], while selected pair correlation function, dihedral and spatial distribution function were obtained by TRAVIS[28,83]. Aggregate analysis delivering clusters size distribution has been performed using the Aggregate software.[84]

Results and Discussion.

The aqueous synthesis route allowed the preparation of clear and uncoloured $[pyr_{13}][IM_{00}]$, $[pyr_{13}][IM_{11}]$, $[pyr_{13}][IM_{22}]$, $[pyr_{13}][IM_{14}]$, as well as $[pyr_{11}][IM_{14}]$ and $[pyr_{14}][IM_{14}]$ with a Li^+, Br^- and H_2O content below 2 ppm. All the studied samples are liquid at ambient conditions (see e.g. ref. [85]).

The physicochemical properties, reported in terms of density, viscosity and ionic conductivity values at different temperatures, are summarized in Table I. [86,87]. The density of the $[pyr_{13}]$-based ionic liquids samples is seen to moderately increase with the steric hindrance of the anion, i.e., a raise of about 15 % in passing from $[IM_{00}]$ (the smallest anion) to $[IM_{14}]$ (the largest one). Also, less than 4 % density decrease is detected moving from 20 to 80 °C, suggesting that temperature slightly affects the ion packing. Conversely, the rheological properties are strongly influenced by the anion size, especially at lower temperatures. For instance, a viscosity from three to seven times higher is observed at 80 and 20 °C, respectively, in passing from $[IM_{00}]$ to $[IM_{14}]$. An opposite trend is displayed by the conductivity, indicating how the ion transport properties are correlated to the rheological one. At 0 °C ion conduction values of the order of 10^{-4} mS cm^{-1} are observed for $[pyr_{13}][IM_{11}]$ and $[pyr_{13}][IM_{22}]$, as these ionic sample are solid below 10 °C whereas $[pyr_{13}][IM_{00}]$ and $[pyr_{13}][IM_{14}]$ are still in their liquid state [87], even if the latter, due to its high viscosity, exhibits a relatively low conductivity.

Table I. Density, viscosity and ionic conductivity values at different temperatures. The (absolute) error on the density is equal to ± 0.001 g cm^{-3} whereas the (related) one on the conductivity is 10 %. Data taken from Refs [86,87].

Ionic liquid sample	Density / g cm^{-3}			Viscosity / mPa s			Conductivity / mS cm^{-1}			
	20 °C	50 °C	80 °C	20 °C	50 °C	80 °C	0 °C	20 °C	50 °C	80 °C
$[pyr_{13}][IM_{00}]$	1.343	1.319	1.296	45 ± 2	21 ± 1	10.6 ± 0.5	2.8	5.5	11.0	18.3
$[pyr_{13}][IM_{11}]$	1.433	1.405	1.379	73 ± 4	23 ± 1	11.3 ± 0.6	0.00075	2.7	6.7	12.0
$[pyr_{13}][IM_{22}]$	1.517	1.486	1.457	200 ± 10	49 ± 3	18.1 ± 0.9	0.00071	0.53	2.2	5.1
$[pyr_{13}][IM_{14}]$	1.546	1.514	1.484	300 ± 20	81 ± 4	28 ± 2	0.067	0.30	1.3	3.5

Figure 1 depicts the molar conductivity *vs*. viscosity dependence as Walden plot [88,89] of the $[pyr_{13}]$-based ionic liquids. The data were calculated from the values reported in Table I whereas the calibration curve (dotted straight line) was determined by a 0.01 N KCl aqueous solution [88]. The pyrrolidinium ionic liquids lie modestly below the ideal Walden line, i.e., indicating favourable conditions [88] as good ion transport properties in conjunction with low viscosity. This suggests

that the [pyr_{13}]-based samples mostly consist of independent mobile ions [23], e.g., formed by cations almost uniformly localized around the anions [90,91].

Figures 2 a)-d) report the whole set of experimental X-ray and neutron scattering data that we collected on the series of available [pyr_{1n}][IM_{xy}] samples, with n=1-4, x=0,1,2 and y=0,1,2,4. Figures 2 a) and c) show Small and Wide Angle X-ray Scattering data, respectively. Figures 2 b) and d) show Small Angle Neutron Scattering data, respectively. In Figure 2 a) the SAXS patterns for [pyr_{11}][IM_{14}] and [pyr_{14}][IM_{14}] are shown, aiming at determining the effect of increasing side alkyl chain at fixed fluorinated chain length, as probed by X-ray; while in Figure 2 c) the SWAXS patterns for [pyr_{13}][IM_{xy}], with (x,y)=(0,0) ([FSI]), (1,1) ([TFSI]), (2,2) ([BETI]) and (1,4) are reported: such a measurements set illustrates the X-ray response to changes in the fluorinated side chain length, at constant alkyl chain size. These figures show that in the low momentum transfer (Q) range ($Q<2$ Å^{-1}) the X-ray diffraction patterns are characterised by the presence of *two* distinct peaks, hereinafter indicated as Q_{II} and Q_{III} in order of increasing Q position.

On the other hand, Figures 2 b) shows the effect of increasing alkyl chain at constant perfluoro alkyl chain as seen by neutron scattering and Figures 2 d) describes how neutron scattering appreciates the structural evolution upon increasing fluorinated side chain length in the anion at constant side alkyl chain in the cation. It is well-known that ILs bearing long enough side alkyl chains are characterised by a distinctly hierarchical morphology at mesoscopic spatial scales [39]. In particular, in a plethora of ILs bearing long enough side alkyl chains, a high level of compartmentalization is observed due to alkyl chains segregation into nm-scale domains that are embedded into the 3-dimensional matrix formed by the charged moieties of cations and anions. [13,39–56] Such a complex structural organization has a direct fingerprint in X-ray and/or neutron scattering patterns that manifests as a low Q peak, hereinafter indicated as Q_I. The position of the latter peak falls at lower Q values than the previously mentioned Q_{II} and Q_{III} peaks. The characteristic size associated to this structural heterogeneity can be estimated as $D\sim 2\pi/Q_I$ and has been found to linearly grow with increasing alkyl chain length. Previous studies on pyrrolidinium-based ([pyr_{1n}] RTILs (when paired with the [IM_{11}] anion) showed that X-ray scattering probes the existence of structural heterogeneities (i.e. it allow appreciating the existence of a low Q peak, associated to the alkyl tails segregation) only for $n\geq 6$. [34,35,92] Below that threshold length, no appreciable scattering feature has been detected. This observation is consistent with the present data sets reported in Figure 2 a) and c), where it appears that SAXS is essentially featureless below 0.7 Å^{-1}. On the other hand Figure 2 b) shows the existence of a distinct low Q peak in the SANS patterns that is centred at ca. 0.45 Å^{-1} in the case of ILs bearing alkyl chains with varying length and a fixed perfluorobutyl side chain in the anion. The position of the latter peak is not affected by the

alkyl chain length and this observation suggests that neutrons detect the existence of nano segregated domains associated to the clustering of fluorous tails.

This is further confirmed by observation of Figure 2 d) where, at fixed side alkyl chain (n=3, propyl) , one varies the fluorous tail on the anion and a progressive development of the Q_I peak occurs upon growing the fluorous chain length: in particular while $[pyr_{13}][IM_{00}]$ and $[pyr_{13}][IM_{11}]$ show featureless diffraction patterns for $Q<0.8$ Å^{-1}, on the contrary, $[pyr_{13}][IM_{22}]$ and $[pyr_{13}][IM_{14}]$ are characterised by noticeable features in that Q range. The former shows a not so well defined and broad peak at ca. 0.6 Å^{-1}, while the latter definitively shows a low Q peak centred at $Q=0.45$ Å^{-1}. This is an indication that analogously with the behaviour observed with alkyl side chains, upon increasing of the side chain length, a low Q peak develops and shifts to lower and lower Q values with increasing chain length. While the X-ray probe does not appreciate the existence of the structural heterogeneities leading to the low Q peak in the present selection of ILs, neutrons are a sensitive probe for such a feature and, accordingly, a low Q peak gets discernible already when the perfluoroalkyl chain is a perfluorobutyl one . Driven by these considerations, we interrogated the Molecular Dynamics simulations conducted on the different RTILs, for their ability to reproduce such effects. Figure 3 shows the level of agreement between X-ray diffraction patterns from $[pyr_{13}][IM_{xy}]$, with (x,y)=(0,0) ([FSI]), (1,1) ([TFSI]), (2,2) ([BETI]) and (1,4) and the corresponding MD-derived quantities. The chosen interatomic potential provides an excellent agreement with the experimental X-ray data sets: all the relevant features are quantitatively accounted for, including the absence of the low Q peak. On the other hand Figure 4 shows that the same potential nicely accounts for the presence of a low Q peak in the neutron diffraction pattern: experimental and computed SANS patterns are shown for $[pyr_{11}][IM_{14}]$ and $[pyr_{13}][IM_{14}]$ (note that no absolute comparison is made for these data sets, as the normalization of SANS data is different from the ones from MD simulations, so data are shown on different ordinate scales). The presence of the low Q peak in the SANS patterns reveals the existence of a nanoscale segregated morphology in ILs bearing a long enough side perfluoro alkyl tail. We explored the morphology of these ILs using different analysis tools, interrogating the MD generated snapshots that have been validating upon comparison with experimental diffraction patterns.

The different size of the probed anions leads to a differentiation of their solvation around the reference cation. Figures 5 show the pair distribution functions (pdf) related to the centers of mass (CoM) of the different ionic species in the series $[pyr_{13}][IM_{xy}]$, with (x,y)=(0,0), (1,1), (2,2) and (1,4). One can appreciate that Cation-Cation (C-C) correlations are not much influenced by the change in the anion nature: first neighbours are located at approximately 7.5 Å, without evident

shift due to the change in anion; nevertheless some effects become apparent when observing larger distances, where the increasing steric obstruction due to the increasing fluorinated tail length determines some expansion of the cation-cation solvation shell, especially for r> 12 Å.

The substantially smaller size of the [IM_{00}] anion, as compared to the other anions, leads to the development of a structured solvation shell of anions around a reference ion (either cation or anion) that manifests itself as a double peak in the Anion-Anion (A-A) pdf at ca. 8 and 10 Å and in a double peak in the Cation-Anion (C-A) pdf at ca. 5 and 6 Å , in the same distance range where other symmetric anions show a single peak; only the IL bearing the [IM_{14}] anion shows a similar splitting in the A-A pdf, presumably due to the anion's largely asymmetrical structure.

This situation can be better rationalised, by inspection of Figure 6 a), where the spatial distribution of neighbour anion's CoM is shown around a reference cation for the [IM_{00}] and [IM_{22}] anions ([IM_{11}] behaves more similarly to [IM_{22}] and is omitted for clarity sake). Therein it is shown that three main lobes constitute the first anion solvation shell around the charged nitrogen atom of the cation. Such lobes have neighbour lobes at slightly larger distance from the reference cation in the case of [IM_{00}] anion (hence the split peak in the corresponding C-A pdf), while larger symmetric anions (such as [IM_{22}]) tend to distribute in their first solvation shell in the space between the two mentioned lobes (hence the position of the first C-A pdf peak for [IM_{22}] at a distance intermediate between the two positions of the split peak in [IM_{00}]). In Figure 6 b), the number of neighbour anions surrounding the reference cation is shown for the case of the symmetric anions: it appears that the first solvation shell (for $r \lesssim 9$ Å) contains a varying number of anions, depending on their size (7.7, 6.9 and 5.8, respectively for [IM_{00}], [IM_{11}] and [IM_{22}]).

Analogously, the small size of the [IM_{00}] anion allows a closer approach of neighbour anions in a structured way, with different approach locations that are only slightly different in distance from the reference anion, thus leading to the double peak in the A-A pdf. The other, larger, anions tend to approach a reference one in a more homogeneous way with a larger closer approach distance.

We next approach mesoscopic correlations in this class of ILs, using a variety of analysis tools to interrogate the MD trajectories on the nature of the nm-scale structural heterogeneities that were detected using neutron scattering techniques.

Using a commonly employed analysis approach developed by the Margulis team [18,82,93–95], we decomposed the computed X-ray and neutron scattering patterns in contributions arising from characteristic alternations occurring in the samples. The mentioned studies and the subsequent ones explained the nature of the commonly observed peaks Q_I, Q_{II} and Q_{III} in ILs. It has been proposed

that they represent the fingerprint of different kinds of pseudo-periodic alternations in the liquid state. In particular, adjacencies, charges and polarities alternations have been demonstrated to be responsible for the appearance of diffraction peaks centred at Q_{III}, Q_{II} and Q_I, respectively. Considering the symmetric anions ([IM_{xx}], x=0-2), we notice in Figure 2 c) that the position of Q_{II} progressively shifts towards lower Q values upon increasing the fluorous moiety size. This implies a progressive expansion of the cation-anion first solvation shell, in agreement with the trend observed in figure 5 b), as due to the increasing steric hindrance of larger and larger anions. The [IM_{14}] anion seems to lead to an intermediate situation, as can be expected due to its bearing two largely different fluorous moieties.

While X-ray data in Figure 2 c) cannot help in discussing the evolution of peak centred at Q_I with x, the neutron scattering data in Figure 2 d) show a distinct shift from a shoulder centred at 0.6 $Å^{-1}$ in [pyr_{13}][IM_{22}] to a clearly distinguishable peak centred at 0.45 $Å^{-1}$ in [pyr_{13}][IM_{14}]. Such peaks are shown in the figure. It can be appreciated that upon increasing the side chain length of the fluorous moiety, the peak shifts towards smaller Q vales. The trend (even the one associated to asymmetric anions) is consistent with previous findings on other ILs concerning both fluorous and non-fluorous chains. Following Margulis' approach [18,82,93–95] we analysed the computed neutron diffraction patterns in terms of alternating polar/apolar moieties and Figure 7 reports this analysis. In particular we show how the computed static structure factor can be decomposed into terms arising from polar/alkyl apolar (Aa) and polar/perfluoroalkyl apolar (Af) alternations. In agreement with previous related literature only salts bearing the [IM_{22}] and the [IM_{14}] anions show a positive Af-Af peak and a negative P-Af peak (both centred at ca. 6 nm^{-1} and 5 nm^{-1} for the two salts, respectively) that lead to an overall non negligible low Q peak in the neutron diffraction patterns. It then clearly appears that while the short propyl chain in the cation is not leading to any substantial Polar/Aa alternation contribution, when the perfuoroalklyl is long enough (i.e. $x \geq 2$, in [IM_{xx}]) the Polar /Af alternation provides a non-negligible contribution, fingerprinting the nanoscale segregation of the fluorinated moieties into separated domains with respect to the charged matrix. To better clarify this effect and the whole context of this paper, we also show in Figure 7 e), the corresponding decomposition of the *X-ray* computed diffraction pattern in terms of the same contributions as above. It appears that the Polar/Af alternation also is detect in this representation, but, due to contrast (that for X-ray is different from neutron scattering) reasons, the overall combination of positive and negative peaks leads to a null total amplitude, in agreement with the experimental data. Accordingly, the fact that X-ray scattering does not appreciate a low Q peak for the case of [IM_{22}] and [IM_{14}] based ILs, does not imply that there is no Polar/Af alternation, but rather that the probe (in this case X-ray) does not succeed in detecting it, due to contrast reasons.

This segregation mechanism can be straightforwardly visualised in Figure 8, using a three colours coding for the three kinds of domain that characterise these triphilic materials, namely charged (yellow), apolar alkyl (red) and apolar perfluoroalkyl (green) moieties have been differently coloured: such a representation directly shows the kind of compartments that develop into these salts, upon increasing the side fluorous chain length.

An alternative and instructive approach to detect the existence of segregated domains into the bulk structure of liquid systems has been proposed by Canongia-Lopes and coworkers, who in a series of papers provided a computationally robust approach to determine the existence of aggregates belonging to a given domain. Assuming that two CH_3-/CF_3- groups belong to the same aggregate (or cluster) when their mutual distance is shorter than 5 or 6 Å (for H or F, respectively), it is possible to interrogate the simulation boxes and extract the population of (either alkyl or perfluoroalkyl) clusters of a given size. In Figure 9, we show such a trend, as a function of the anion's nature. It appears that methyl groups tend to cluster in the case of salts with the [IM_{00}] and [IM_{11}] anions, but the largest size achieved is ca. 12 and 10 members each. On the other hand the perfluoromethyl moieties tend to cluster in the case of salts with the [IM_{22}] and [IM_{14}] anions and while in the [IM_{22}]-based salt the clusters reach a size of ca. 22 moieties, in the case of the [IM_{14}]-based salt, the fluorous domain percolates across the simulation box, as indicated by the cluster size approaching the total number of CF_3 groups in the simulation box (800).

Conclusion.

In this contribution we reported a characterization of the complex morphology features in a series of pyrrolidinium-based ILs bearing a fluorinated anion, with high interest as electrolyte media for lithium battery applications. The synergic exploitation of complementary X-ray and Neutron scattering techniques and Molecular Dynamics simulations allows extracting precise structural information at atomistic level. The complementarity of the scattering techniques turns to be fundamental to assess specific structural features in this class of ILs: while X-ray scattering does not appreciate mesoscopic scale spatial organization, Neutron scattering instead allows detecting the existence of segregated domains built up by the anion's perfluoroalkyl moieties. MD simulations can accurately reproduce such a situation and allow the achievement of an atomistic description of the segregation mechanism.

Acknowledgement.

AT and OR gratefully acknowledge access to the Japan Synchrotron Radiation Research Institute (JASRI-Spring8) and the kind and skilful support from Dr. S. Kohara in exploiting beamline BL04B2. This research also used resources of the Advanced Photon Source, a U.S. Department of Energy (DOE) Office of Science User Facility operated for the DOE Office of Science by Argonne National Laboratory under Contract No. DE-AC02-06CH11357. AT and OR acknowledge the competent support from Dr. B. Aoun in exploiting beamline 11-ID-C at APS. We acknowledge Helmholtz Zentrum Berlin (HZB) for the allocation of SANS neutron beamtime. This work has been supported by the University of Rome Sapienza Project: "Microscopic and mesoscopic organization in ionic liquid-based systems." (RG11715C7CC660BE).

References

[1] D.A. Notter, M. Gauch, R. Widmer, P. Wager, A. Stamp, R. Zah, H.-J. Althaus, Environ. Sci. Technol. 44 (2010) 6550.

[2] H. Yang, S. Amiruddin, H.J. Bang, Y.K. Sun, J. Prakash, J. Ind. Eng. Chem. 12 (2006) 12.

[3] C. Chiappe, D. Pieraccini, J. Phys. Org. Chem. 18 (2005) 275.

[4] R.P. Swatloski, S.K. Spear, J.D. Holbrey, R.D. Rogers, J. Am. Chem. Soc. 124 (2002) 4974.

[5] H. Ohno, Electrochemical Aspects of Ionic Liquids, Wiley-Interscience, Hoboken/New Jersey, 2005.

[6] G.B. Appetecchi, M. Montanino, S. Passerini, in:, Ion. Liq. Sci. Appl., American Chemical Society, 2012, pp. 4–67.

[7] T.M. Bandhauer, S. Garimella, T.F. Fuller, J. Electrochem. Soc. 158 (2011) R1.

[8] J.-W. Park, K. Ueno, N. Tachikawa, K. Dokko, M. Watanabe, J. Phys. Chem. C 117 (2013) 20531.

[9] T. Kuboki, T. Okuyama, T. Ohsaki, N. Takami, J. Power Sources 146 (2005) 766.

[10] J.S. Moreno, G. Maresca, S. Panero, B. Scrosati, G.B. Appetecchi, Electrochem. Commun. 43 (2014) 1.

[11] A. Triolo, O. Russina, B. Fazio, G.B. Appetecchi, M. Carewska, S. Passerini, J. Chem. Phys. 130 (2009).

[12] O. Russina, F. Lo Celso, N. Plechkova, C.J.C.J. Jafta, G.B.G.B. Appetecchi, A. Triolo, F. Lo, C. Natalia, Top. Curr. Chem. 375 (2017) 58.

[13] O. Russina, F. Lo Celso, M. Di Michiel, S. Passerini, G.B. Appetecchi, F. Castiglione, A. Mele, R. Caminiti, A. Triolo, Faraday Discuss. 167 (2013) 499.

[14] F. Castiglione, M. Moreno, G. Raos, A. Famulari, A. Mele, G.B. Appetecchi, S. Passerini, J. Phys. Chem. B 113 (2009) 10750.

[15] F. Lo Celso, Y. Yoshida, F. Castiglione, M. Ferro, A. Mele, C.J. Jafta, A. Triolo, O. Russina, Phys. Chem. Chem. Phys. 19 (2017) 13101.

[16] F. Lo Celso, G.B. Appetecchi, C.J. Jafta, L. Gontrani, J.N. Canongia Lopes, A. Triolo, O. Russina, J. Chem. Phys. 148 (2018) 193816.

[17] Y. Shen, D.F. Kennedy, T.L. Greaves, A. Weerawardena, R.J. Mulder, N. Kirby, G. Song, C.J. Drummond, Phys. Chem. Chem. Phys. 14 (2012) 7981.

[18] J.J. Hettige, J.C. Araque, C.J. Margulis, J. Phys. Chem. B 118 (2014) 12706.

[19] A.B. Pereiro, J.M.M. Araújo, S. Martinho, F. Alves, S. Nunes, A. Matias, C.M.M. Duarte, L.P.N. Rebelo, I.M. Marrucho, ACS Sustain. Chem. Eng. 1 (2013) 427.

[20] O. Palumbo, F. Trequattrini, G.B. Appetecchi, L. Conte, A. Paolone, J. Mol. Liq. 243 (2017) 9.

[21] M. Kunze, E. Paillard, S. Jeong, G.B. Appetecchi, M. Sch, M. Winter, S. Passerini, J. Phys.

Chem. C 115 (2011) 19431.

[22] D.R. MacFarlane, P. Meakin, J. Sun, N. Amini, M. Forsyth, J. Phys. Chem. B 103 (1999) 4164.

[23] I. Bandres, D.F. Montano, I. Gascon, P. Cea, C. Lafuente, Electrochim. Acta 55 (2010) 2252.

[24] T.L. Merrigan, E.D. Bates, S.C. Dorman, J.H. Davis, Chem. Commun. (2000) 2051.

[25] D. Almantariotis, A.S. Pensado, H.Q.N.N. Gunaratne, C. Hardacre, A.A.H.H. Pádua, J.-Y. Coxam, M.F. Costa Gomes, J. Phys. Chem. B 121 (2017) 426.

[26] D. Almantariotis, T. Gefflaut, a a H. Pádua, J.-Y. Coxam, M.F. Costa Gomes, J. Phys. Chem. B 114 (2010) 3608.

[27] G.D. Smith, O. Borodin, J.J. Magda, R.H. Boyd, Y. Wang, J.E. Bara, S. Miller, D.L. Gin, R.D. Noble, Phys. Chem. Chem. Phys. 12 (2010) 7064.

[28] O. Hollóczki, M. Macchiagodena, H. Weber, M. Thomas, M. Brehm, A. Stark, O. Russina, A. Triolo, B. Kirchner, ChemPhysChem 16 (2015) 3325.

[29] A.B. Pereiro, M.J. Pastoriza-Gallego, K. Shimizu, I.M. Marrucho, J.N.C. Lopes, M.M. Piñeiro, L.P.N. Rebelo, J. Phys. Chem. B 117 (2013) 10826.

[30] N.S.M. Vieira, P.M. Reis, K. Shimizu, O.A. Cortes, I.M. Marrucho, J.N.C. Lopes, A.B. Pereiro, L.P.N. Rebelo, V.A. Online, N.S.M. Vieira, P.M. Reis, K. Shimizu, O.A. Cortes, I.M. Marrucho, J.N.C. Lopes, A.B. Pereiro, L.P.N. Rebelo, N. De Lisboa, U. De Lisboa, V.A. Online, N.S.M. Vieira, P.M. Reis, K. Shimizu, O.A. Cortes, I.M. Marrucho, J.N.C. Lopes, A.B. Pereiro, L.P.N. Rebelo, RSC Adv. 5 (2015) 65337.

[31] M.L. Ferreira, M.J. Pastoriza-Gallego, J.M.M. Araújo, J.N. Canongia Lopes, L.P.N. Rebelo, M. M. Piñeiro, K. Shimizu, A.B. Pereiro, J. Phys. Chem. C 121 (2017) 5415.

[32] K. Shimizu, A.A. Freitas, J.N. Canongia Lopes, J. Mol. Liq. 226 (2017) 28.

[33] C.S. Santos, N.S. Murthy, G. a Baker, E.W. Castner, J. Chem. Phys. 134 (2011) 121101.

[34] S. Li, J. Leobardo, J. Guo, L. Anovitz, G. Rother, R.W. Shaw, P.C. Hillesheim, S. Dai, G. a. Baker, P.T. Cummings, J.L. Bañuelos, J. Guo, L. Anovitz, G. Rother, R.W. Shaw, P.C. Hillesheim, S. Dai, G. a. Baker, P.T. Cummings, J. Phys. Chem. Lett. 3 (2012) 125.

[35] H.K. Kashyap, C.S. Santos, N.S. Murthy, J.J. Hettige, K. Kerr, S. Ramati, J. Gwon, M. Gohdo, S.I. Lall-ramnarine, J.F. Wishart, C.J. Margulis, E.W. Castner, S.I. Lall-, J.F. Wishart, C.J. Margulis, E.W. Castner, S.I. Lall-ramnarine, J.F. Wishart, C.J. Margulis, E.W. Castner, J. Phys. Chem. B 117 (2013) 15328.

[36] X. Paredes, J. Ferna, A.H. Pa, B. Kirchner, A.S. Pensado, C. Universite, (2014).

[37] S. Sharma, A. Gupta, H.K. Kashyap, (2016).

[38] K. Pilar, V. Balédent, M. Zeghal, P. Judeinstein, S. Jeong, S. Passerini, M. Zeghal, P. Judeinstein, S. Jeong, 031102 (2018).

[39] A. Triolo, O. Russina, H.-J. Bleif, E. Di Cola, J. Phys. Chem. B 111 (2007) 4641.

[40] M. Macchiagodena, F. Ramondo, A. Triolo, L. Gontrani, R. Caminiti, J. Phys. Chem. B 117 (2013) 473.

[41] O. Russina, A. Triolo, L. Gontrani, R. Caminiti, J. Phys. Chem. Lett. 3 (2012) 27.

[42] O. Russina, F. Lo Celso, M. Di Michiel, S. Passerini, G.B. Appetecchi, F. Castiglione, A. Mele, R. Caminiti, A. Triolo, Faraday Discuss. 167 (2013) 499.

[43] R. Atkin, G.G. Warr, J. Phys. Chem. B 112 (2008) 4164.

[44] R. Hayes, S. Imberti, G.G. Warr, R. Atkin, Phys. Chem. Chem. Phys. 13 (2011) 3237.

[45] R. Hayes, S. Imberti, G.G. Warr, R. Atkin, Phys. Chem. Chem. Phys. 13 (2011) 13544.

[46] K. Fujii, S. Kohara, Y. Umebayashi, (2015).

[47] K. Fujii, R. Kanzaki, T. Takamuku, Y. Kameda, S. Kohara, M. Kanakubo, M. Shibayama, S. Ishiguro, Y. Umebayashi, J. Chem. Phys. 135 (2011) 244502.

[48] X. Song, H. Hamano, B. Minofar, R. Kanzaki, K. Fujii, Y. Kameda, S. Kohara, M. Watanabe, S. Ishiguro, Y. Umebayashi, J. Phys. Chem. B 116 (2012) 2801.

[49] A. Triolo, O. Russina, B. Fazio, R. Triolo, E. Di Cola, Chem. Phys. Lett. 457 (2008) 362.

[50] L. Gontrani, O. Russina, F. Lo Celso, R. Caminiti, G. Annat, A. Triolo, J. Phys. Chem. B 113 (2009) 9235.

[51] O. Russina, A. Triolo, L. Gontrani, R. Caminiti, D. Xiao, L.G. Hines Jr., R.A. Bartsch, E.L. Quitevis, N. Plechkova, K.R. Seddon, J. PHYSICS-CONDENSED MATTER 21 (2009).

[52] A. Triolo, O. Russina, B. Fazio, G.B. Appetecchi, M. Carewska, S. Passerini, J. Chem. Phys. 130 (2009) 164521.

[53] E. Bodo, L. Gontrani, R. Caminiti, N. V Plechkova, K.R. Seddon, A. Triolo, J. Phys. Chem. B 114 (2010) 16398.

[54] O. Russina, L. Gontrani, B. Fazio, D. Lombardo, A. Triolo, R. Caminiti, Chem. Phys. Lett. 493 (2010) 259.

[55] M. Macchiagodena, L. Gontrani, F. Ramondo, A. Triolo, R. Caminiti, J. Chem. Phys. 134 (2011).

[56] C. Hardacre, J.D. Holbrey, C.L. Mullan, T.G. a Youngs, D.T. Bowron, J. Chem. Phys. 133 (2010) 074510.

[57] O. Russina, L. Celso, A. Triolo, Phys. Chem. Chem. Phys. 17 (2015) 29496.

[58] F. Lo Celso, A. Triolo, L. Gontrani, O. Russina, J. Chem. Phys. 148 (2018) 1.

[59] M. Montanino, F. Alessandrini, S. Passerini, G.B. Appetecchi, Electrochim. Acta 96 (2013) 124.

[60] M. De Francesco, E. Simonetti, G. Gorgi, G.B. Appetecchi, Challenges 8 (2017).

[61] S. Kohara, K. Suzuya, Y. Kashihara, N. Matsumoto, N. Umesaki, I. Sakai, Nucl. Instruments Methods Phys. Res. Sect. A Accel. Spectrometers, Detect. Assoc. Equip. 467–468 (2001) 1030.

[62] A. Ohmura, K. Sato, N. Hamaya, M. Isshiki, Y. Ohishi, Phys. Rev. B 80 (2009) 054201.

[63] B. Aoun, A. Goldbach, S. Kohara, J.-F. Wax, M.A. Gonzalez, M.-L. Saboungi, J. Phys. Chem. B 114 (2010) 12623.

[64] D.T. Cromer, J. Chem. Phys. 50 (1969) 4857.

[65] A.P. Hammersley, S.O. Svensson, M. Hanfland, A.N. Fitch, D. Hausermann, High Press. Res. 14 (1996) 235.

[66] X. Qiu, J.W. Thompson, S.J.L. Billinge, J. Appl. Crystallogr. 37 (2004) 678.

[67] U. Keiderling, A. Wiedenmann, Phys. B 213–214 (1995) 895.

[68] R. Gilles, U. Keiderling, P. Strunz, A. Wiedenmann, H. Fuess, Mater. Sci. Forum 321–3 (2000) 264.

[69] U. Keiderling, Appl. Phys. A Mater. Sci. Process. 74 (2002) s1455.

[70] B. Hess, C. Kutzner, D. Van Der Spoel, E. Lindahl, J. Chem. Theory Comput. 4 (2008) 435.

[71] D. Van Der Spoel, E. Lindahl, B. Hess, G. Groenhof, A.E. Mark, H.J.C. Berendsen, J. Comput. Chem. 26 (2005) 1701.

[72] J.N. Canongia Lopes, J. Deschamps, A.A.H. Padua, J. Phys. Chem. B 108 (2004) 2038.

[73] J.N. Canongia Lopes, A.A.H. Pádua, Theor. Chem. Acc. 131 (2012) 1129.

[74] J.N. Canongia Lopes, A.A.H. Padua, J. Phys. Chem. B 108 (2004) 16893.

[75] K. Shimizu, D. Almantariotis, M.F.C. Gomes, A.A.H. Pádua, J.N. Canongia Lopes, J. Phys. Chem. B 114 (2010) 3592.

[76] C.E.S. Bernardes, A. Joseph, J. Phys. Chem. A 119 (2015) 3023.

[77] G. Bussi, D. Donadio, M. Parrinello, J. Chem. Phys. 126 (2007) 014101.

[78] M. Parrinello, A. Rahman, J. Appl. Phys. 52 (1981) 7182.

[79] T. Darden, D. York, L. Pedersen, J. Chem. Phys. 98 (1993) 10089.

[80] U. Essmann, L. Perera, M.L. Berkowitz, T. Darden, H. Lee, L.G. Pedersen, J. Chem. Phys. 103 (1995) 8577.

[81] J.D. Hunter, Comput. Sci. Eng. 9 (2007) 90.

[82] H.K. Kashyap, J.J. Hettige, H.V.R. Annapureddy, C.J. Margulis, Chem. Commun. 48 (2012) 5103.

[83] M. Brehm, B. Kirchner, J. Chem. Inf. Model. 51 (2011) 2007.

[84] C.E.S. Bernardes, J. Comput. Chem. 38 (2017) 753.

[85] M. Kunze, S. Jeong, E. Paillard, M. Winter, S. Passerini, J. Phys. Chem. C 14 (2010) 12364.

[86] Q. Zhou, W. a Henderson, G.B. Appetecchi, M. Montanino, S. Passerini, J. Phys. Chem. B 112 (2008) 13577.

[87] G.B. Appetecchi, M. Montanino, M. Carewska, M. Moreno, F. Alessandrini, S. Passerini, Electrochim. Acta 56 (2011) 1300.

[88] W. Xu, E.I. Cooper, C.A. Angell, J. Phys. Chem. B 107 (2003) 6170.

[89] D.R. MacFarlane, M. Forsyth, E.I. Izgorodina, A.P. Abbott, G. Annat, K. Fraser, Phys. Chem. Chem. Phys. 11 (2009) 4962.

[90] M. Videa, W. Xu, B. Geil, R. Marzke, C.A. Angell, J. Electrochem. Soc. 148 (2001) A1352.

[91] H. Every, A.G. Bishop, M. Forsyth, D.R. MacFarlane, Electrochim. Acta 45 (2000) 1279.

[92] C.S. Santos, N.S. Murthy, G.A. Baker, E.W. Castner, C.S. Santos, N.S. Murthy, G.A. Baker, E.W. Castner, 121101 (2011).

[93] H.V.R. Annapureddy, H.K. Kashyap, P.M. De Biase, C.J. Margulis, J. Phys. Chem. B 114 (2010) 16838.

[94] H.K. Kashyap, C.S. Santos, R.P. Daly, J.J. Hettige, N.S. Murthy, H. Shirota, E.W. Castner, C.J. Margulis, J. Phys. Chem. B 117 (2013) 1130.

[95] J.C. Araque, J.J. Hettige, C.J. Margulis, J. Phys. Chem. B 119 (2015) 12727.

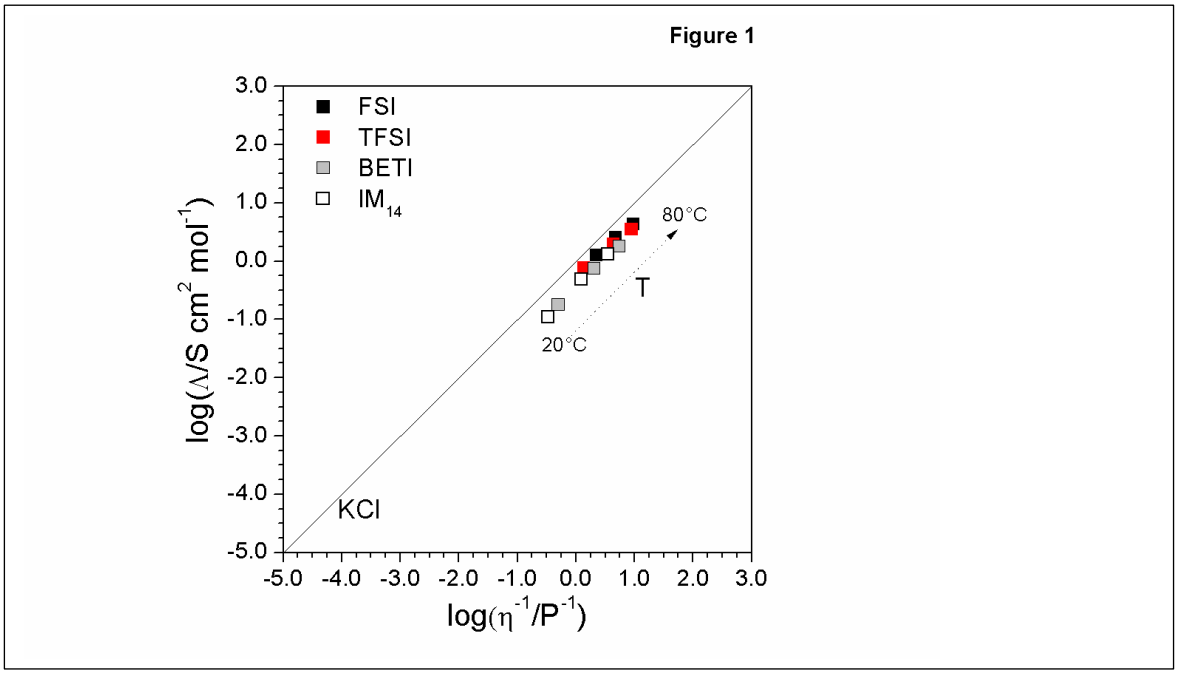

Figure 1. Molar conductivity vs. viscosity dependence as Walden plot of the four ionic liquids: [pyr_{13}][IM_{00}], [pyr_{13}][IM_{11}], [pyr_{13}][IM_{22}], [pyr_{13}][IM_{14}].

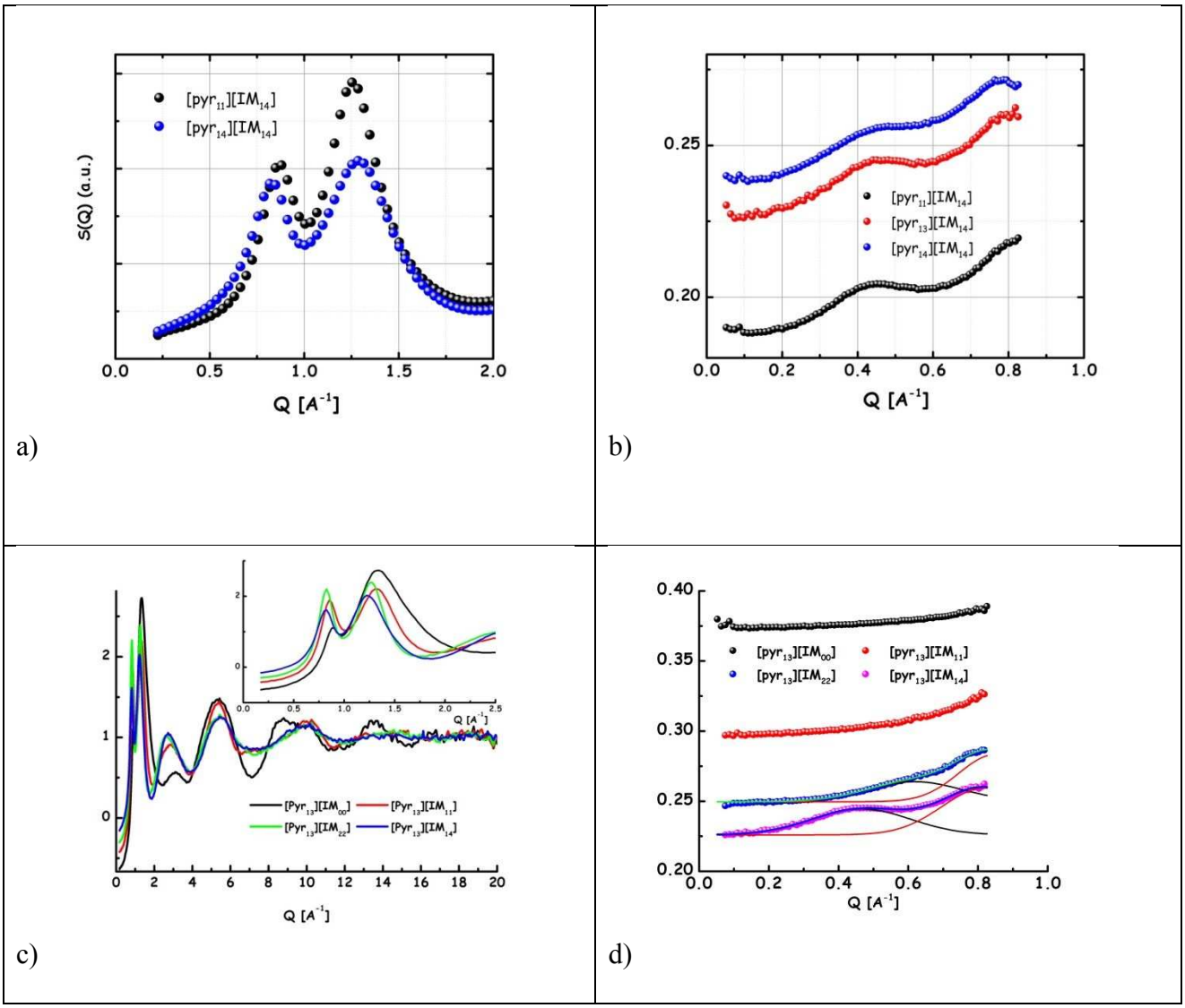

Figure 2. a) Small Angle X-ray scattering patterns for $[pyr_{11}][IM_{14}]$ and $[pyr_{14}][IM_{14}]$, at ambient conditions; b) Small Angle Neutron scattering patterns for $[pyr_{11}][IM_{14}]$, $[pyr_{13}][IM_{14}]$ and $[pyr_{14}][IM_{14}]$, at ambient conditions (the vertical shift is a consequence of the different amount of incoherent scattering background); c) Small-Wide Angle X-ray scattering patterns for $[pyr_{13}][IM_{00}]$, $[pyr_{13}][IM_{11}]$, $[pyr_{13}][IM_{22}]$ and $[pyr_{13}][IM_{14}]$, at ambient conditions. In the inset the Small Angle portion of the data sets is highlighted; d) Small Angle Neutron scattering patterns for $[pyr_{13}][IM_{00}]$, $[pyr_{13}][IM_{11}]$, $[pyr_{13}][IM_{22}]$ and $[pyr_{13}][IM_{14}]$, at ambient conditions (the vertical shift is a consequence of the different amount of incoherent scattering background). For the latter two ILs, a fitting of the data in terms of two Gaussian functions is included, highlighting the shift of the positions of the low Q peak, Q_I, with increasing fluorous chain length.

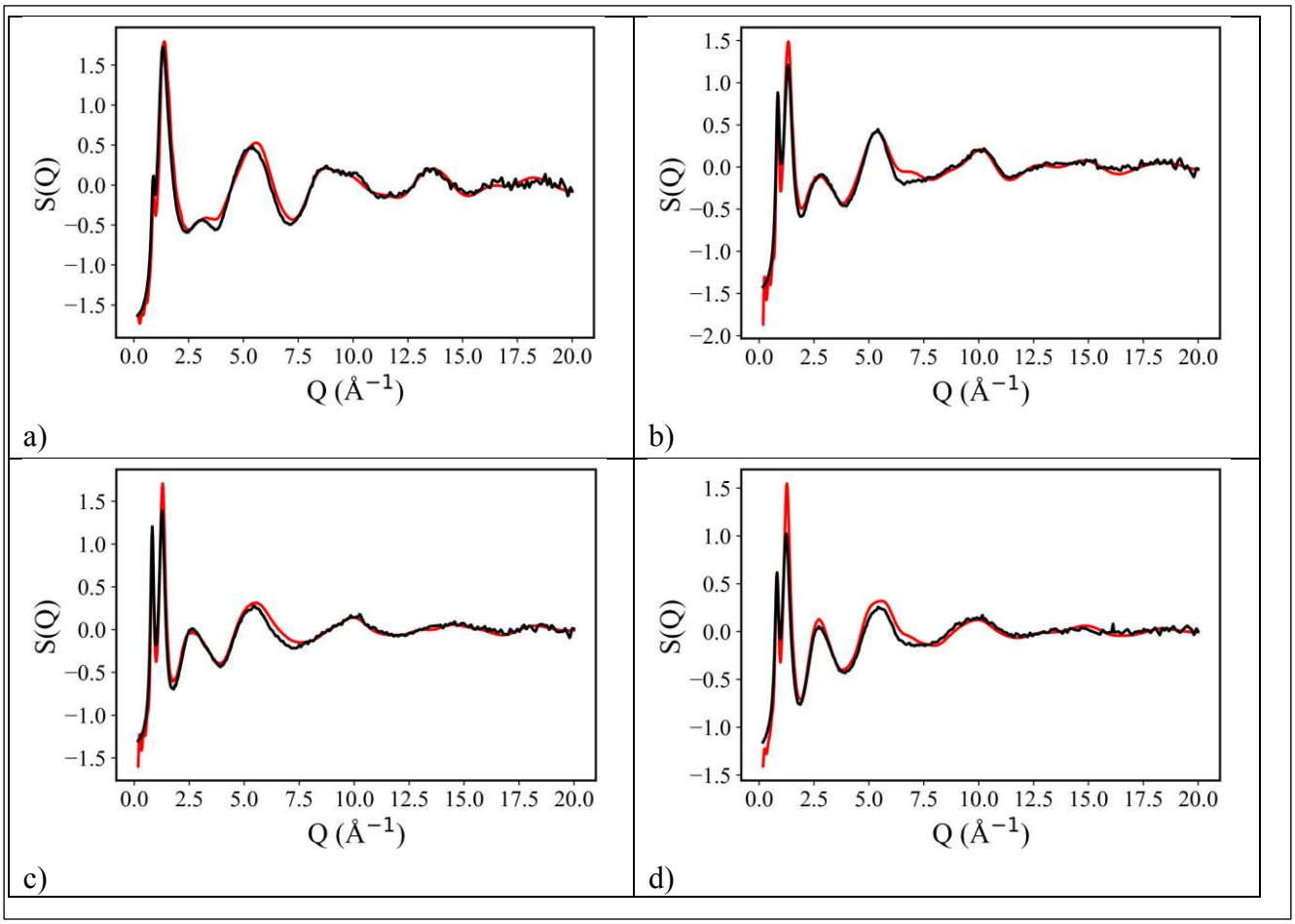

Figure 3. Comparison of the experimental (black lines) Small-Wide Angle X-ray scattering patterns for a) [pyr$_{13}$][IM$_{00}$], b) [pyr$_{13}$][IM$_{11}$], c) [pyr$_{13}$][IM$_{22}$] and d) [pyr$_{13}$][IM$_{14}$], at ambient conditions and the corresponding quantities obtained from presently reported Molecular Dynamics simulations (red lines).

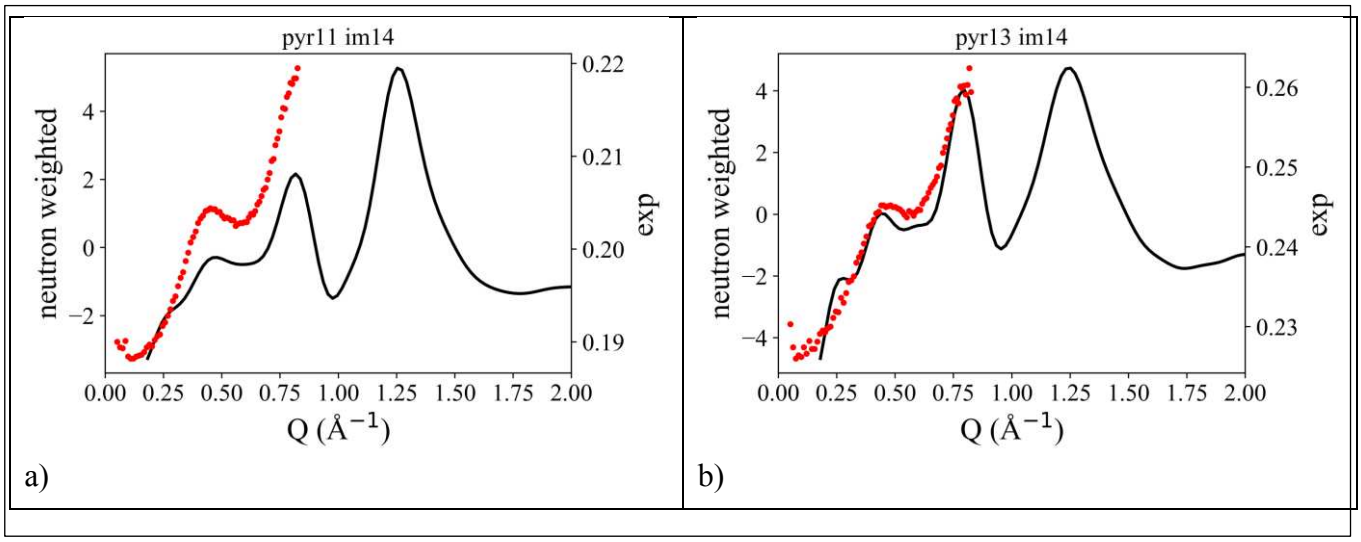

Figure 4. Comparison of the experimental (red symbols) Small Angle Neutron scattering patterns for a) [pyr_{11}] [IM_{14}] and b) [pyr_{13}][IM_{14}], at ambient conditions and the corresponding quantities obtained from presently reported Molecular Dynamics simulations (black lines; note the different ordinate scales).

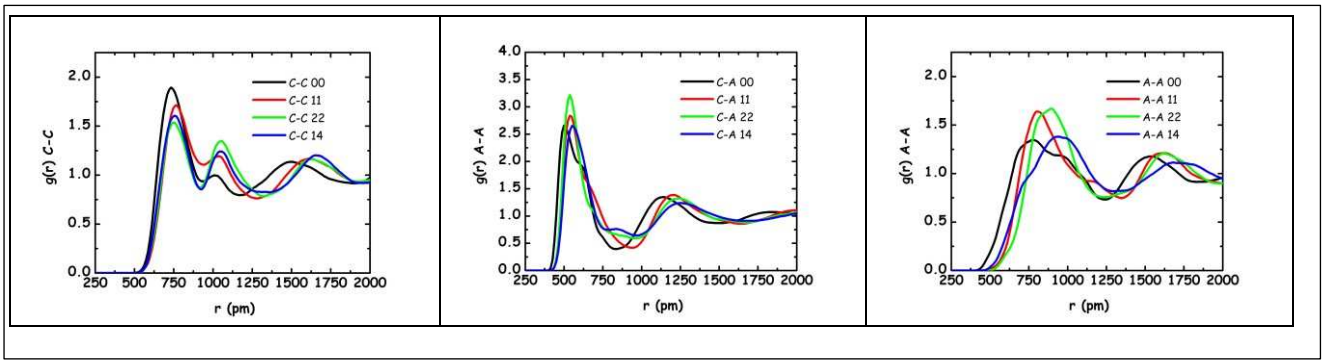

Figure 5. MD computed Pair Distribution Functions, g(r), for the ionic Centers of Mass for Cation-Cation (C-C, left panel), Cation-Anion (C-A, center panel) and Anion-Anion (A-A, right panel) ions for the series of ILs: $[pyr_{13}][IM_{00}]$, $[pyr_{13}][IM_{11}]$, $[pyr_{13}][IM_{22}]$ and $[pyr_{13}][IM_{14}]$, at ambient conditions.

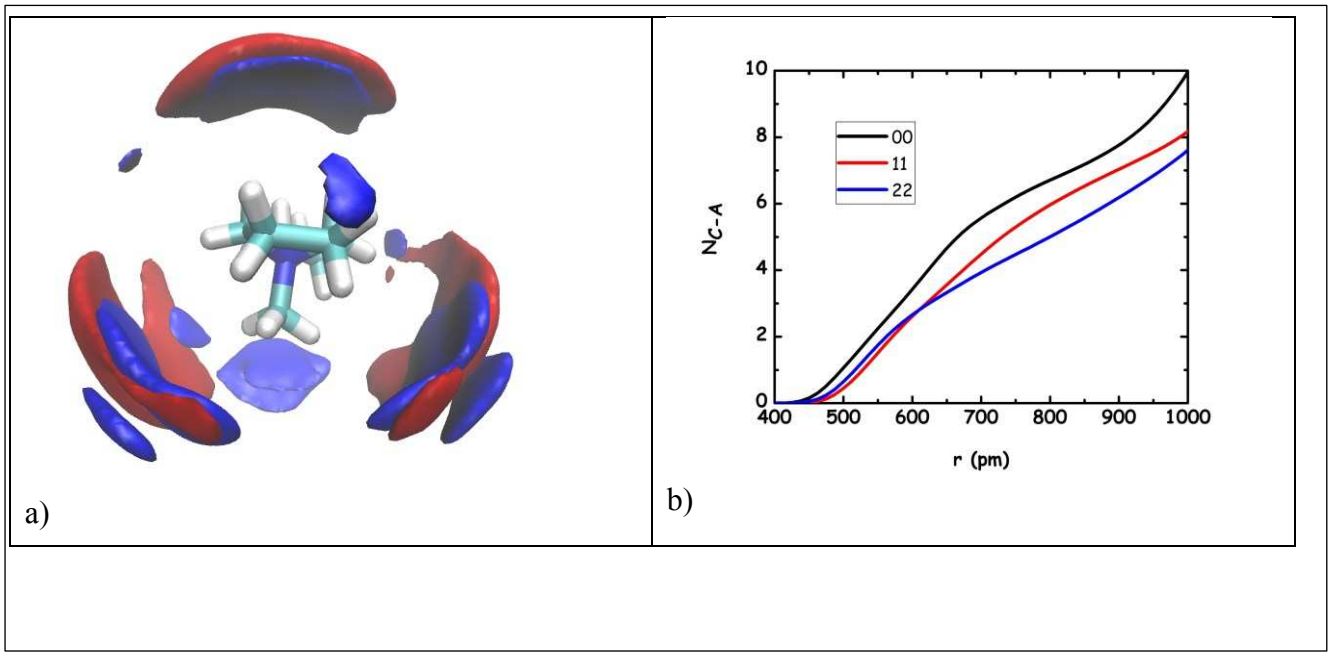

Figure 6. a) MD-derived Spatial Distribution Function of neighbour anion's Center of Mass around a reference cation for the cases of [IM_{00}] (blue) and [IM_{22}] (red) anions; b) MD-derived number of neighbour anions surrounding a reference cation for the case of the symmetric anions [IM_{00}], [IM_{11}] and [IM_{22}].

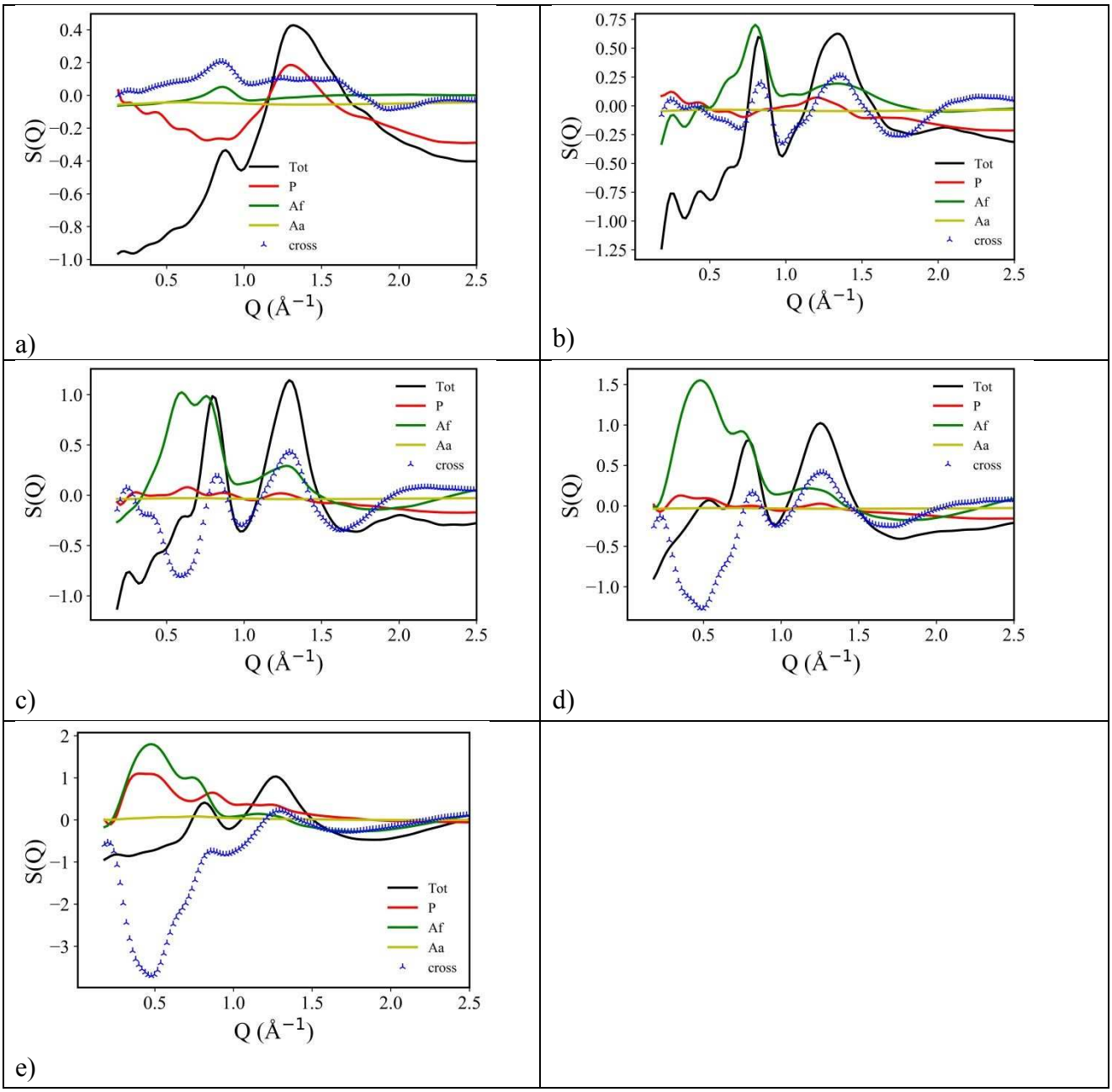

Figure 7. a)-d) MD derived decomposition of the neutron-weighted scattering patterns for a) [pyr_{13}][IM_{00}], b) [pyr_{13}][IM_{11}], c) [pyr_{13}][IM_{22}] and d) [pyr_{13}][IM_{14}], at ambient conditions, in terms of polar (P), apolar alkyl (Aa) and apolar fluorous (Af) contributions and resulting cross term (Cross). e) MD derived decomposition of the X-ray-weighted scattering patterns for [pyr_{13}][IM_{14}], at ambient conditions, in terms of polar (P), apolar alkyl (Aa) and apolar fluorous (Af) contributions and resulting cross term (Cross).

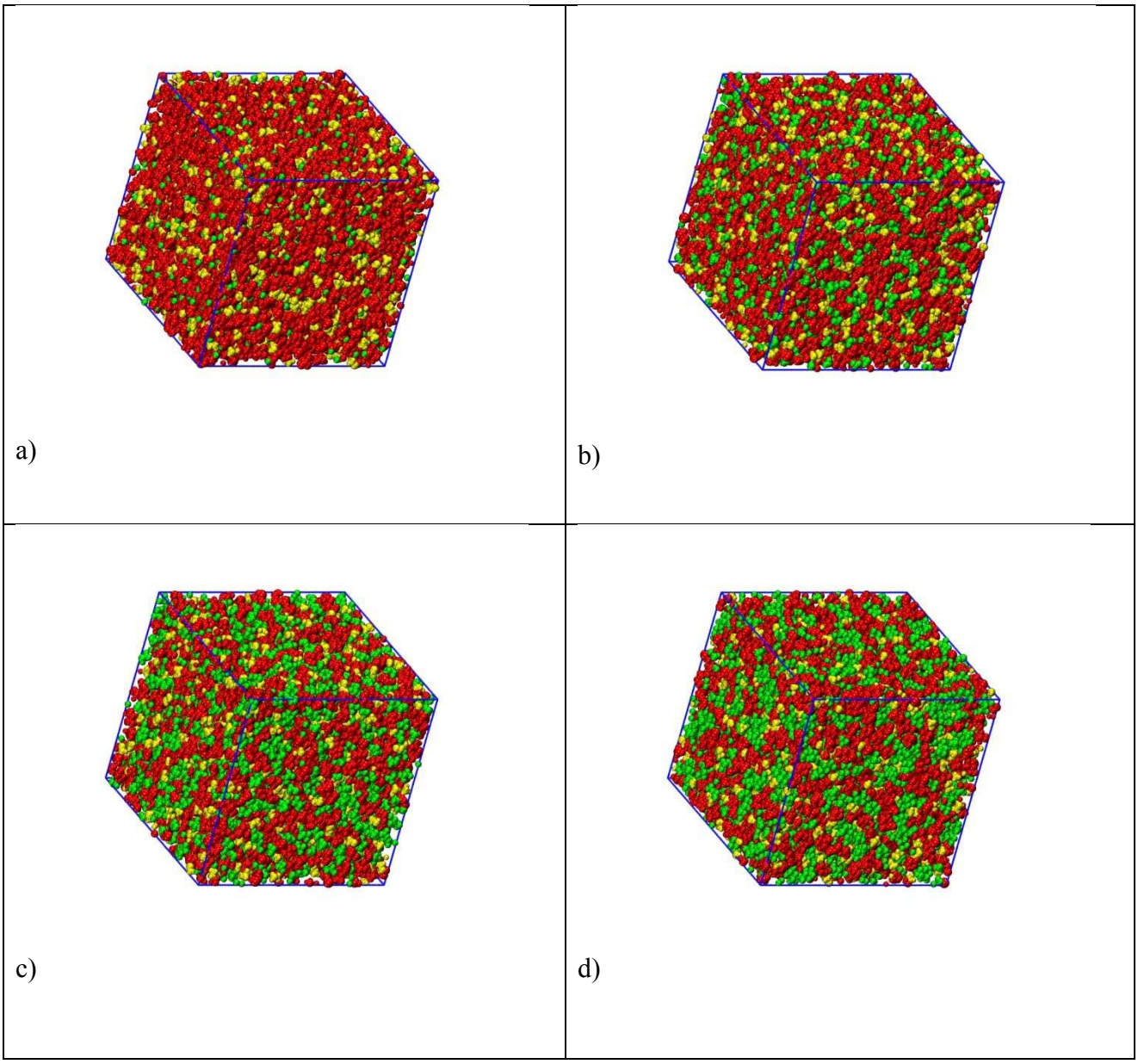

Figure 8. Representative MD simulation boxes for a) [pyr_{13}][IM_{00}], b) [pyr_{13}][IM_{11}], c) [pyr_{13}][IM_{22}] and d) [pyr_{13}][IM_{14}], at ambient conditions, using a three colours coding for the charged (yellow), apolar alkyl (red) and apolar perfluoroalkyl (green) moieties.

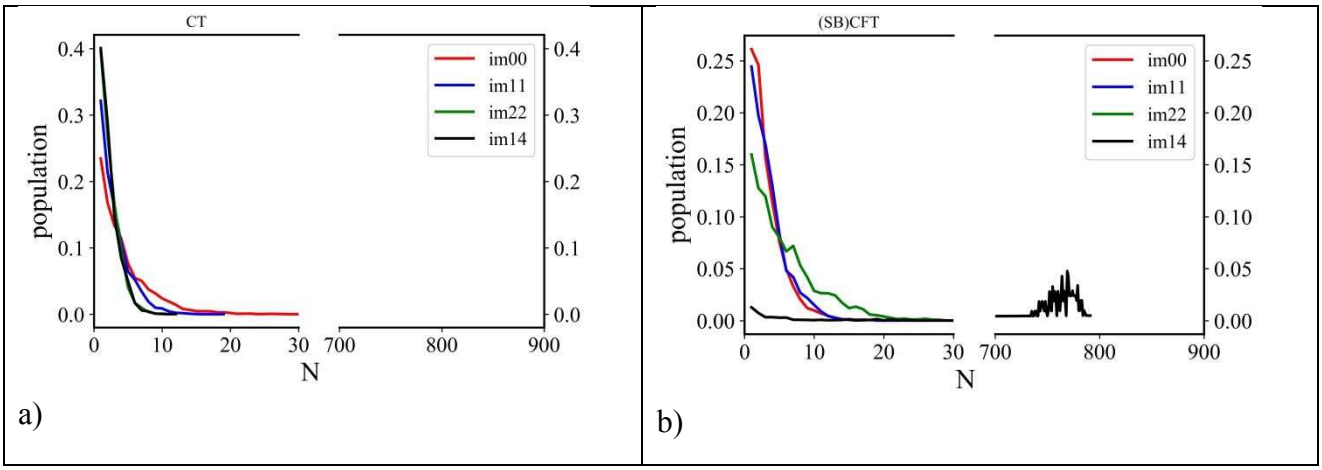

Figure 9. MD-derived size distribution of aggregates composed of a) terminal methyl groups belonging to the cation propyl chains and b) terminal perfluoromethyl groups belonging to the anion chains for $[pyr_{13}][IM_{00}]$, $[pyr_{13}][IM_{11}]$, $[pyr_{13}]$ $[IM_{22}]$ and $[pyr_{13}][IM_{14}]$, at ambient conditions (in the case of the $[IM_{00}]$, the fluorine atoms are considered).